PAPER

Cite this: *RSC Adv.*, 2019, **9**, 26487

MoS₂ nanotubes loaded with TiO₂ nanoparticles for enhanced electrocatalytic hydrogen evolution†

Bo Feng,[a] Chuntao Liu, [iD] *[ab] Weiyi Yan,[a] Jianxin Geng[a] and Guimin Wang[a]

Efficient and stable non-precious metal catalysts composed of earth-abundant elements are crucial to the hydrogen evolution reaction (HER) in high-energy conversion efficiency. Herein, TiO₂/MoS₂-NTs catalyst, in which the MoS₂ nanotubes were loaded with TiO₂ nanoparticles, have been synthesized *via* a facile solvothermal and hydrothermal method. The as-prepared TiO₂/MoS₂-NTs electrocatalyst demonstrated enhanced electrocatalytic hydrogen evolution performance compared with MoS₂-NTs. Electrochemical measurements reveal the overpotential and Tafel slope of as-prepared TiO₂/MoS₂-NTs are −0.21 V and 42 mV dec^{-1}. The HER improvement is proposed to be attributed to the increased edge sites results from the interfaces and synergic effect between TiO₂ nanoparticles and MoS₂ nanotubes.

Introduction

The sustained and rapid development of human society has brought a growing demand for energy. Traditional fossil energy sources are difficult to meet green, healthy and sustainable energy development trends, their limited reserves and environmental pollution problems have stimulated extensive research on clean and renewable alternative energy.[1] As a fuel, hydrogen possesses clean, renewable, portable properties and the highest energy density per unit mass among all chemical fuels, and has been considered to be an essential sustainable and environmentally-friendly energy source.[2,3] There are currently three main technologies, including steam methane reforming, coal gasification and water electrolysis for industrial hydrogen production.[4] Water electrolysis is an unquestionable clean way of energy utilization, since its feedstock is water—an abundant and renewable resource.[5] It is critical to maximize the hydrogen evolution reaction (HER) efficiency by utilizing the excellent cathode catalysts. Platinum (Pt) and other precious metals are reported to be the most efficient HER electrocatalysts as their small overpotential and high electrocatalytic activity, whereas the high cost and relative scarcity of noble metals prohibit their practical application.[6–8] Therefore, developing efficient and cheap non-precious metal HER catalysts

composed of earth-abundant elements have a great significance on the electrocatalytic hydrogen production.[9–12]

Molybdenum disulphide (MoS₂), a typical layered structure with weak van der Waals interactions between individual sandwiched S–Mo–S layers, has been widely investigated as an efficient alternative to platinum for HER because of its promising electrochemical activity and abundant distribution.[13–15] However, its HER performance is greatly limited by the insufficient active sites and intrinsic poor conductivity.[16–19] On the basis of the above two key factors, extensive efforts have been devoted to the improvement of either the number of active sites or conductivity of MoS₂ by cooperation with conductive materials and morphology optimization (controlling the synthesis of well-defined morphology with nanostructures) during the past few years.[20–22] As is well-known that the characteristic surface morphology and/or microstructure of MoS₂ manipulates the electron transport and electrolyte diffusion. MoS₂ nanotubes (MoS₂-NTs) were utilized widely because of more exposed edge sites and higher specific area for the HER.[23–27] However, the overall HER activity is still limited as generally only a small fraction of edge sites contribute to the reaction rate.[28–30] Titanium dioxide (TiO₂) is rather inexpensive, relatively non-toxic, and excellent physical and chemical stability in acidic media.[31–34] Most of the MoS₂/TiO₂ hetero-structures such as nanoflowerlike MoS₂@TiO₂ nanohybrids,[35,36] TiO₂ nanoparticles supported MoS₂ nanosheet,[37] TiO₂/g-C₃N₄/MoS₂ nanocomposites,[38] MoS₂/TiO₂ thin film[39,40] and TiO₂@MoS₂ nanotube array[41] were used to improve the electrocatalytic hydrogen evolution activity and photocatalytic reaction. As for HER, loading TiO₂ on MoS₂ support cannot only activate the sites of MoS₂ nanotubes, but also utilizes high mobility MoS₂ frame as a bridge for charge transport.[42]

Herein, we demonstrate a facile solvothermal and hydrothermal method to load TiO₂ nanoparticles onto MoS₂-NTs for

[a]*School of Chemistry and Materials Science, Heilongjiang University, Harbin 150080, PR China. E-mail: liuct@hlju.edu.cn; liu_chuntao@163.com*

[b]*Key Laboratory of Chemical Engineering Process & Technology for High-efficiency Conversion, School of Chemistry and Materials Science, Heilongjiang University, Harbin 150080, PR China*

† Electronic supplementary information (ESI) available: Survey XPS spectrum and SEM image of TiO₂/MoS₂-NTs, TEM image of MoS₂-NTs, LSV polarization curves and corresponding Tafel plots of different catalysts, CV curves at various scan rates of different catalysts. See DOI: 10.1039/c9ra05041h

the HER. This electrocatalyst exhibited an onset overpotential of 140 mV, a Tafel slope of 42 mV dec^{-1}, and an exchange current density of 32.4 μA cm^{-2}. Electrochemical tests illustrated the catalytic efficiency is greatly improved by more edge sites results from the interfaces and synergic effect between TiO$_2$ nanoparticles and MoS$_2$ nanotubes.

Experimental section

Chemical and reagents

Sodium molybdate dihydrate (Na$_2$MoO$_4$·2H$_2$O), thiourea ((NH$_2$)$_2$CS), tetrabutyltitanate (C$_{16}$H$_{36}$O$_4$Ti), anhydrous ethanol, octylamine, nitric acid (HNO$_3$) were purchased from Sinopharm Chemical Reagent Co. Ltd., China. All chemicals and reagents were used as received without further purification. All the chemicals are analytical reagents.

Preparation of MoS$_2$-NTs catalysts

MoS$_2$-NTs were fabricated by a facile solvothermal method. In a typical synthesis, Na$_2$MoO$_4$·2H$_2$O and (NH$_2$)$_2$CS (Mo/S molar ratio of 1 : 4) were dissolved in 60 mL mixture of anhydrous ethanol/octylamine (v/v = 1 : 1) followed by stirring for about 30 min at room temperature to form a homogeneous solution. This solution was transferred into a 100 mL sealed Teflon-lined stainless steel autoclave and heated at 200 °C for 24 h in an electric oven. After the autoclave was cooled to room temperature naturally, the resulting black product was collected by centrifugation and washed repeatedly with deionized water and ethanol to remove ions and possible remnants. Finally, the MoS$_2$-NTs were dried in a vacuum oven at 60 °C overnight before characterizations and further preparation.

Preparation of TiO$_2$/MoS$_2$-NTs catalyst

TiO$_2$/MoS$_2$-NTs catalysts were prepared *via* a simple hydrothermal method. Briefly, 2 M HNO$_3$ was initially added into 140 mL mixture of water/ethanol (v/v = 1 : 4) until its pH reached to 2. Then, a certain amount of MoS$_2$-NTs were dispersed in this solution followed by continuous stirring for 30 min at room temperature. After that, 4 mL of anhydrous ethanol solution which contained 0.5 mL of tetrabutyltitanate (TBT) was slowly injected into the abovementioned solution at 75 °C. The reaction mixture was capped and maintained at 75 °C for 24 h under vigorous stirring. After cooling down to room temperature, the product was washed thoroughly with anhydrous ethanol and deionized water. Finally, the homemade catalyst was dried in a vacuum oven at 60 °C for 12 h for further characterization and test. The weight percentage of TiO$_2$ at 5, 10 and 15 wt% were evaluated for supporting MoS$_2$-NTs and denoted as TiO$_2$/MoS$_2$-5, TiO$_2$/MoS$_2$-10 and TiO$_2$/MoS$_2$-15, respectively. For comparison, pure TiO$_2$ nanoparticles were synthesized under the same conditions in the absence of MoS$_2$-NTs.

Characterizations

X-ray diffraction (XRD) measurements were performed on a Bruker D8 diffractmeter with Cu Kα radiation (λ = 1.5406 Å).

The operation voltage and current was 40 KV and 150 mA, respectively. X-ray photoelectron spectroscopy (XPS) measurements were carried out on Kratos-AXISULTRADLD, with Al Kα (1486.6 eV) radiation. The binding energies were referenced to the C 1s line at 284.6 eV from adventitious carbon. Raman spectra were collected on a Jobin Yvon HR 800 micro-Raman spectroscopy system with excitation line of 532 nm. The morphologies and microstructures were characterized by the scanning electron microscopy (SEM) and transmission electron microscopy (TEM).

Electrochemical measurements

All electrochemical measurements were performed on an electrochemical workstation (CHI 760E, China) in a conventional three-electrode electrochemical cell at 25 ± 0.2 °C. A glassy carbon (GC) electrode (4 mm in diameter) with catalysts was used as the working electrode. A Pt wire and Hg/Hg$_2$SO$_4$ electrode were used as the counter and reference electrode, respectively. All the potentials reported in this manuscript were calibrated with respect to reversible hydrogen electrode (RHE).

The catalysts were loaded onto the GC electrode by coating slurry method in the following way: 6 mg of catalysts were dispersed into the mixture solution of 0.05 mL Nafion solution (5 wt%, DuPont) and 0.95 mL ethanol by ultrasonication for about 1 h to form a homogeneous ink. Then, 6 μL of the suspension was transferred onto the surface of GC electrode and dried at room temperature, leading to a nominal catalyst loading of 0.286 mg cm^{-2}.

The hydrogen evolution reaction (HER) activity of catalysts was investigated in 0.5 M H$_2$SO$_4$ electrolyte by linear potential sweep voltammetry (LSV) at a scan rate of 5 mV s^{-1}. To evaluate the durability of catalyst, chronopotentiometry experiments were conducted in 0.5 M H$_2$SO$_4$ at a constant density of −10 mA cm^{-2}. The long-term stability of the catalysts was performed by continuous 2000 cyclic voltammetry (CV) scanning between −0.6 V and 0.6 V at a scan rate of 50 mV s^{-1}. Electrochemical impedance spectra (EIS) were carried out at overpotential of −200 mV over a frequency ranging from 100 kHz to 0.01 Hz with 12 points per decade. CV curves were used to estimate the double-layer capacitance (C_{dl}) under the potential region of 0.35–0.45 V performed with various sweep rates (20, 40, 60, 80 and 100 mV s^{-1}). The electrolyte solution was deaerated with ultrapure argon for at least 30 min before each electrochemical measurement.

Results and discussion

The XRD patterns of TiO$_2$, MoS$_2$-NTs and TiO$_2$/MoS$_2$-NTs composites are shown in Fig. 1. For MoS$_2$-NTs, it is obviously observed that diffraction peaks at 2θ = 14.3°, 33.5°, 39.3° and 58.9° correspond to (002), (101), (103) and (110) lattice planes of the hexagonal phase MoS$_2$ (JCPDS#37-1492), respectively. For pure TiO$_2$, six characteristic XRD peaks are found at 2θ = 25.4°, 37.9°, 48.5°, 54.6°, and 62.8°, which are ascribed to (101), (004), (200), (105) and (204) lattice planes of the anatase phase TiO$_2$ (JCPDS #21-1272), respectively. The diffraction peaks of TiO$_2$/
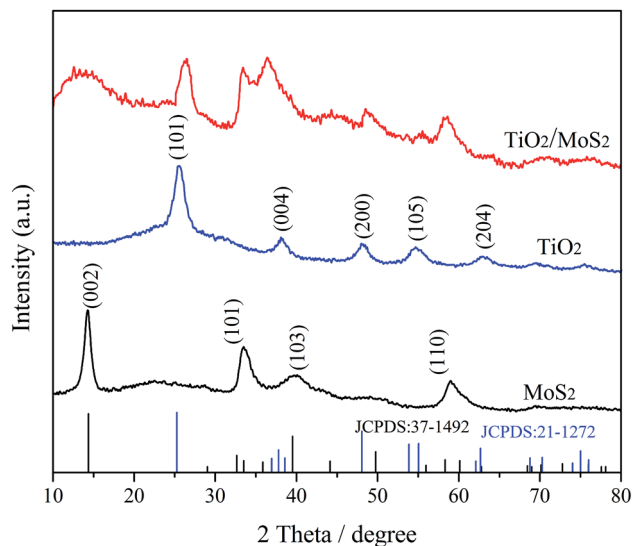
Fig. 1 XRD patterns of TiO₂, MoS₂-NTs and TiO₂/MoS₂-NTs.

MoS₂-NTs composites match those of TiO₂ and MoS₂, revealing that the hybrid compound was successfully prepared.

Raman spectra were carried out for further characterizing the crystalline of TiO₂, MoS₂-NTs and TiO₂/MoS₂-NTs composites in Fig. 2. The two dominant Raman scattering peaks of pure MoS₂ can be observed at 383 and 404 cm⁻¹ corresponding to the in-plane E_{2g}^1 and out-of-plane A_{1g} modes, respectively.[43–45] Additionally, the integral intensity of the A_{1g} mode is twice than that of the E_{2g}^1 mode, indicating that the MoS₂-NTs are rich of edge sites.[42] The characteristic Raman peaks of pure TiO₂ at 143, 395, 517 and 637 cm⁻¹ are assigned to the E_g^1, B_{1g}^1, $A_{1g} + B_{1g}^1$ and E_g^2 modes of anatase-phase TiO₂, respectively, and the strongest peak at 143 cm⁻¹ is the symmetric stretching modes of O–Ti–O. The characteristic vibration peaks of TiO₂ and MoS₂ co-existed in the Raman spectrum of TiO₂/MoS₂-NTs composites,

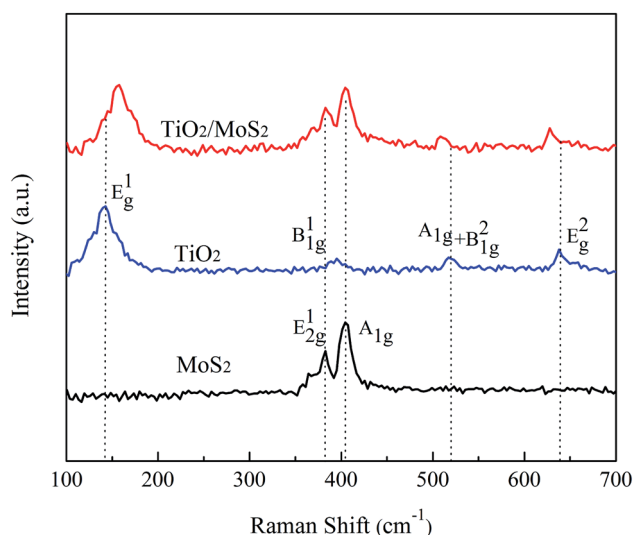indicating that the TiO₂/MoS₂-NTs composites were successfully prepared. However, the wavenumber and intensity of the characteristic peaks of TiO₂/MoS₂-NTs composites changed slightly. The E_g^1 mode showed a significant blue shift, while the $A_{1g} + B_{1g}$ and E_g^2 modes oppositely have a slightly red shift in the Raman spectrum of TiO₂/MoS₂-NTs composites compared with the corresponding peaks of TiO₂. Remarkably, the obvious shift of the related peaks for TiO₂/MoS₂-NTs composites is consistent with the results of Liu[46] and demonstrated that coupling effect between MoS₂ and TiO₂. Moreover, the two strong peaks of the E_{2g}^1 and A_{1g} for MoS₂ masked the B_{1g}^1 peak of TiO₂ in the Raman spectrum of TiO₂/MoS₂-NTs composites. This is mostly owed to the relatively small content of TiO₂.

The morphology and structure of the TiO₂/MoS₂-NTs can be characterized by SEM and TEM. Fig. 3a and S1† displayed the SEM image of TiO₂/MoS₂-NTs. It is very clear that TiO₂ nanoparticles dispersed on surface of the MoS₂-NTs to form TiO₂/MoS₂-NTs in Fig. 3b. MoS₂-NTs surface is attached by a small amount of TiO₂ nanoparticles in the TEM image of as-prepared TiO₂/MoS₂-NTs, as shown in Fig. 3c, comparing with the naked MoS₂-NTs (Fig. S2†). Fig. 3d is the high-resolution TEM image of TiO₂/MoS₂-NTs sample, there are two different lattice spacing, the one lattice spacing is 0.35 nm, which matches with that of anatase TiO₂ (101) planes, the other lattice spacing of 0.62 nm is correspond to the lattice spacing of (002) planes for MoS₂ nanotubes. TEM images confirmed a well decorated of TiO₂ nanoparticles on MoS₂-NTs, suggesting the formation of TiO₂/MoS₂-NTs composites which may be beneficial to the improvement of HER performance.[37]

The electrocatalytic HER activities of all prepared samples can be observed by LSV in acidic solution. Fig. 4a showed the LSV polarization curves of MoS₂-NTs, TiO₂, Pt/C, and TiO₂/
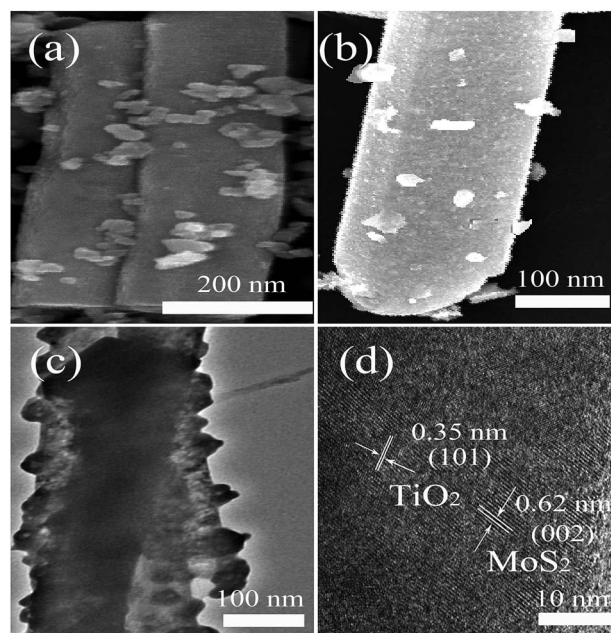

Fig. 3 SEM images (a and b) and TEM images (c and d) of as-prepared TiO₂/MoS₂-NTs.

Fig. 2 Raman spectra of TiO₂, pristine MoS₂-NTs and TiO₂/MoS₂-NTs.
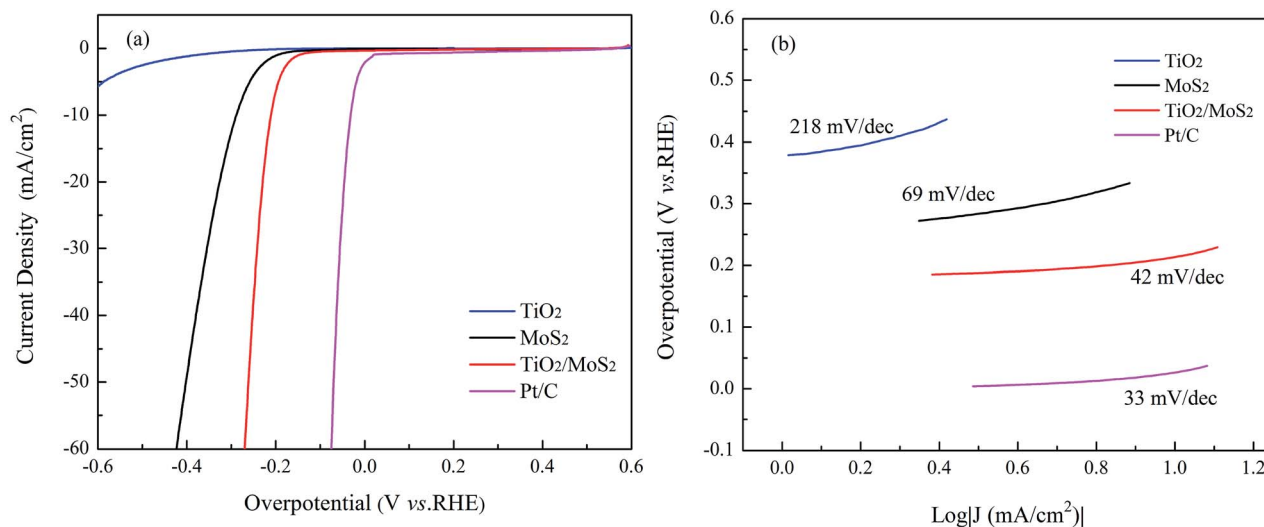
Fig. 4 (a) Polarization curves and (b) the corresponding Tafel plots of TiO_2, MoS_2-NTs and TiO_2/MoS_2-NTs in 0.5 M H_2SO_4 solution.

MoS_2-NTs in 0.5 M H_2SO_4 solution at 25 °C. The TiO_2 showed poor electrocatalytic HER activity, which contributed negligibly to the performances of the integrated electrodes. Comparing with that of MoS_2-NTs, TiO_2/MoS_2-NTs displayed the more positive onset overpotential of 0.14 V, which favored the mass transfer and subsequently reduced the concentration polarization,[47] indicating a good catalytic activity to the product. It is well known that the electrocatalyst with a lower overpotential is typically considered to have a better catalytic activity at the same current density. The TiO_2/MoS_2-NTs composites only required a overpotential of down to 0.21 V to achieve a cathodic current density of 10 mA cm^{-2}, much lower than that of the MoS_2-NTs (0.32 V). Shifting of the overpotential to a small value for TiO_2/MoS_2-NTs further confirmed the improved electrocatalytic HER activity.

The linear portions of the Tafel plots are fitted to the Tafel equation as shown in Fig. 4b. Clearly, the Tafel slopes of TiO_2, MoS_2-NTs, TiO_2/MoS_2-NTs and Pt/C are 218, 69, 42 and 33 mV dec^{-1}, respectively. According to the explanation of Chorkendorff et al.,[7,17] the Tafel slope of Volmer, Heyrovsky and Tafel reaction correspond to 116, 38 and 29 mV dec^{-1}, respectively. The Tafel slope of TiO_2/MoS_2-NTs is much lower than those of TiO_2 or MoS_2-NTs, indicating it's predominate Volmer–Heyrovsky mechanism[33] in which the rate-determining step is the electrochemical desorption of H_{ads} (i.e. Heyrovsky reaction) and superior activity during the HER process. Therefore, the improved HER activities of TiO_2/MoS_2-NTs mainly results from the strong electronic and chemical coupling between highly stable TiO_2 nanoparticles and electroactive MoS_2-NTs. Furthermore, TiO_2/MoS_2-NTs shows a larger exchange current density (j_0) value of 32.4 μA cm^{-2} than MoS_2-NTs (18.7 μA cm^{-2}), which also can corroborate the superior HER performance and faster electron transfer kinetics for the TiO_2/MoS_2-NTs hybrid catalyst. Moreover, we also compared the activity of TiO_2/MoS_2-NTs with those of other HER catalysts reported in the literature (Table 1). The onset overpotential of TiO_2/MoS_2-NTs is smaller

than those of TiO_2/MoS_2 composites. The Tafel slope and overpotential to reach a cathodic current density of 10 mA cm^{-2} of this work exhibit smaller than other six catalysts. The smaller overpotential and Tafel slope imply its excellent electrocatalytic activity. Among them, the exchange current density of TiO_2/MoS_2-NTs is the largest, showing the highest activity.

The XPS measurements were employed to investigate the surface chemical composition and valence state of prepared samples. The wide-scan XPS spectra (Fig. S3†) revealed that the existence of O, Ti, Mo, and S elements in the TiO_2/MoS_2-NTs composites, while a trace of C is from the XPS instrument itself. The binding energy of Mo $3d_{3/2}$ and Mo $3d_{5/2}$ in Fig. 5a are located at 232.4 and 228.8 eV, respectively, indicating that the oxidation state of Mo^{4+} in the pure MoS_2.[48,49,52] After introducing TiO_2 nanoparticles, the peaks of Mo 3d shifted by about 0.3 eV to the lower energy direction, which can be attributed to the electronic interactions between TiO_2 and MoS_2-NTs.[43,50,55] In addition, the characteristic peak of S 2s also appeared at a binding energy of 225.7 eV in the TiO_2/MoS_2-NTs composites. As shown in Fig. 5b, the S peaks located at 162.8 and 161.6 eV represent S $2p_{1/2}$ and S $2p_{3/2}$, respectively, suggesting that S^{2-} existed in the pure MoS_2.[51,54] For TiO_2/MoS_2-NTs, the S $2p_{1/2}$ and S $2p_{3/2}$ peaks are shifted to 162.5 and 161.4 eV. Meanwhile, the S $2p_{3/2}$ energy at 163.3 eV in the TiO_2/MoS_2-NTs composites revealed the existence of bridging S_2^{2-} or apical S^{2-}, which are more beneficial in the HER performance.[10,52,56] According to the literature description,[35] the binding energies of Ti $2p_{1/2}$ and Ti $2p_{3/2}$ peaks in the pure TiO_2 locate at 464.3 and 458.5 eV, respectively. While the TiO_2/MoS_2-NTs composites the Ti $2p_{1/2}$ and Ti $2p_{3/2}$ peaks are shifted to 464.5 and 458.7 eV in Fig. 5c, higher than the corresponding values of pure TiO_2. The shift of peaks indicated possible new bond Ti–O–Mo and the electronic interaction between TiO_2 and MoS_2.[23,53] As shown in Fig. 5d, besides the O 1s peaks at 529.7 eV attributed to the Ti–O–Ti bond, the absorption peaks at 530.9 and 531.5 eV correspond to surface hydroxyl group (Ti–O–H) and adsorbed water,

Table 1 Comparison of the activity displayed by the composites in present work with those of other HER catalysts reported in the literature

Catalyst	η_{onset} (mV $vs.$ RHE)	η_{10} (mV $vs.$ RHE)	Tafel slope (mV dec^{-1})	j_0 (μA cm^{-2})	Ref.
MoS$_2$ nanosheets	120	—	50	12.6	14
MoS$_2$ nanosheets	120	—	55	8.91	28
MoS$_2$@TiO$_2$	130	—	80	25.1	35
MoS$_2$@TiO$_2$	300	340	81	—	36
MoS$_2$/TiO$_2$	—	285	46	—	37
MoS$_2$/TiO$_2$-H	153	—	66.9	—	43
TiO$_2$/MoS$_2$-NTs	140	210	42	32.4	This work

respectively. The O 1s peak at around 530.3 eV is observed, which might be ascribed to the formation of the Ti–O–Mo bonds between MoS$_2$ and TiO$_2$.[36,55]

Durability and long-term stability is another significant factor to evaluate the performance of the electrocatalyst. Chronopotentiometry experiments were conducted to investigate the HER durability of the electrocatalysts in 0.5 M H$_2$SO$_4$. As shown in Fig. 6a, in the initial period for the time-dependent curve of TiO$_2$/MoS$_2$-NTs composites, there is a sharp drop in

overpotential due to the slow desorption of the adsorbed hydrogen atom on the catalysts. The only slightly fluctuation of the overpotential was observed as time changed. There is a small reduction of 20 mV in the overpotential after 24 h, suggesting the excellent durability of the TiO$_2$/MoS$_2$-NTs catalyst. The striking stability was further proved by the LSV polarization curves before and after processing 2000 CV cycles in the same electrolyte. As shown in Fig. 6b, the negligible degradation of HER activity between the curves measured at the initial cycle
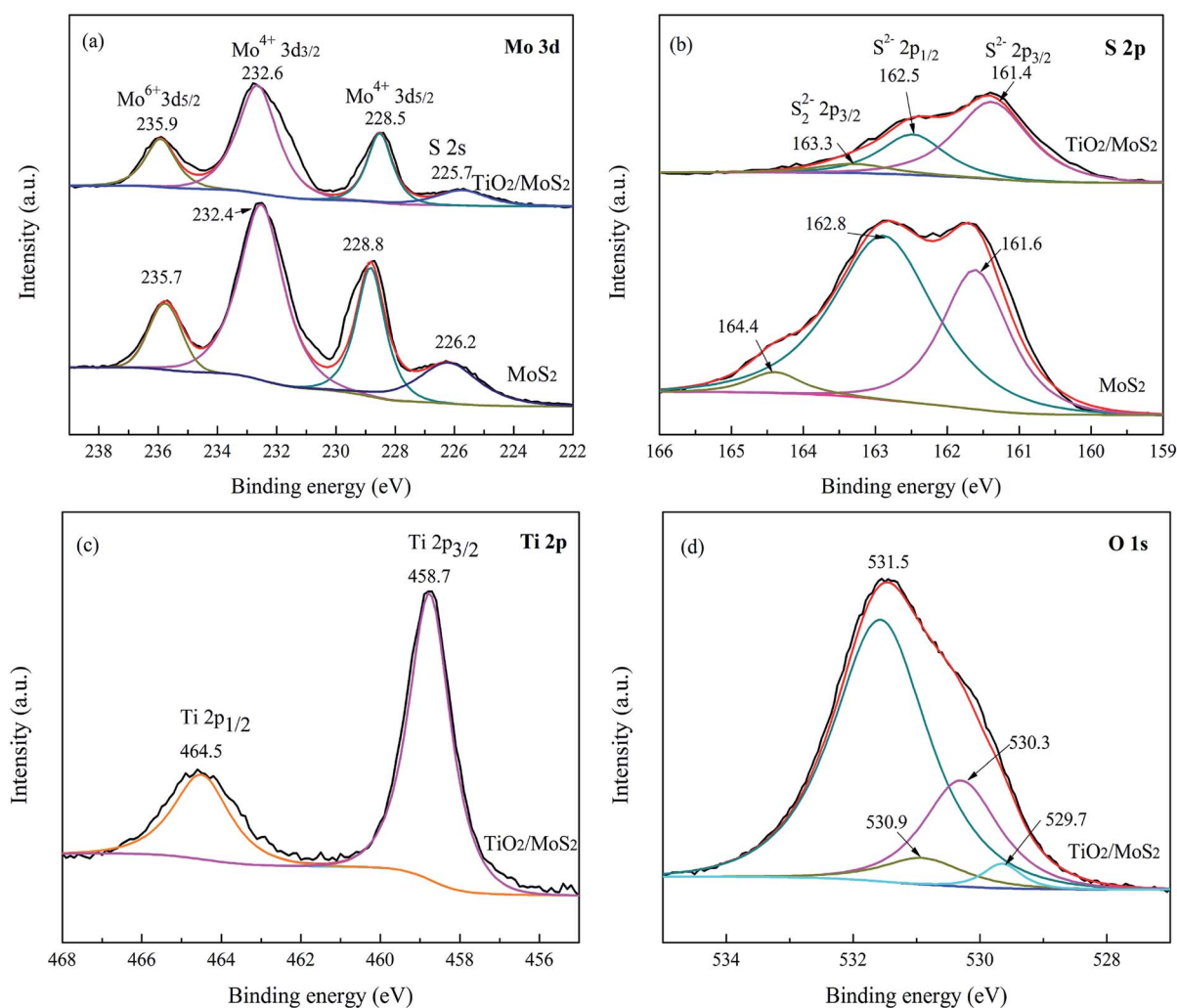
Fig. 5 High-resolution XPS spectra of (a) Mo 3d, (b) S 2p for TiO$_2$/MoS$_2$-NTs and MoS$_2$-NTs, (c) Ti 2p and (d) O 1s spectra of TiO$_2$/MoS$_2$-NTs.
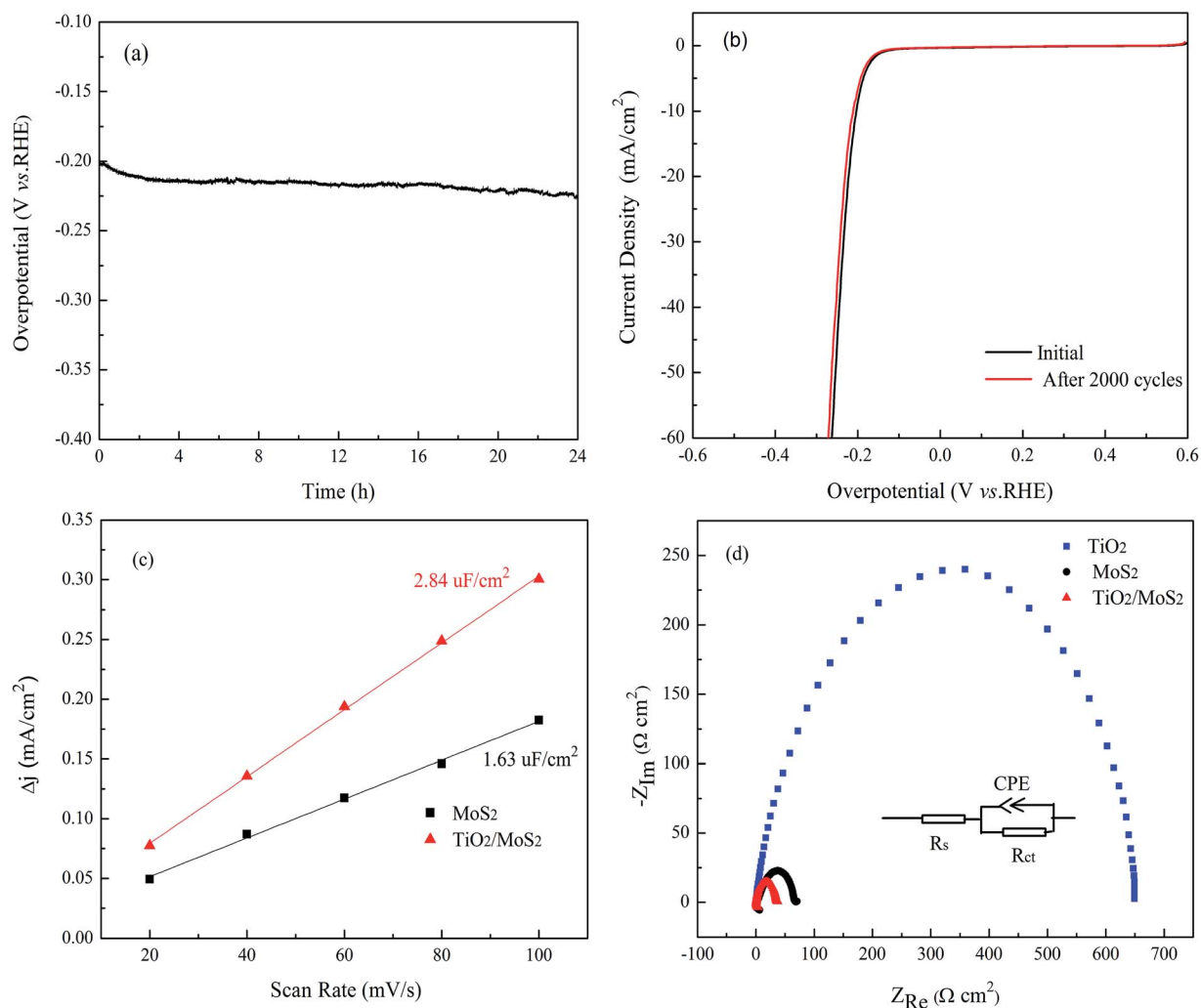
Fig. 6 (a) Chronopotentiometric curve recorded at a constant cathodic current density of −10 mA cm^{-2} and (b) cycling stability test for TiO$_2$/MoS$_2$-NTs. (c) Linear fitting of the capacitive current densities *versus* scanning rates of MoS$_2$-NTs and TiO$_2$/MoS$_2$-NTs electrodes calculated. (d) Nyquist plots of various samples as indicated for the HER process in a 0.5 M aqueous H$_2$SO$_4$ solution at −0.2 V at 25 °C.

and after 2000 CV cycles, indicating the excellent long-term cycling stability of TiO$_2$/MoS$_2$-NTs catalyst.

The higher activity as well as good stability of the TiO$_2$/MoS$_2$-NTs for HER can be attributed to the following reasons. The small size and highly uniform distribution of TiO$_2$ nanoparticles can increase the number of catalytic edge sites that play an important role for HER performance by activating the inert basal planes of MoS$_2$-NTs catalyst. The electrochemical C_{dl} are measured *via* CV method (Fig. S6†) to evaluate the density of active sites of various catalysts, which can be estimated from the slopes of the current density *vs.* scan rate curves.[35] As shown in Fig. 6c, TiO$_2$/MoS$_2$-NTs exhibited much larger C_{dl} of 2.84 μF cm^{-2} than that of MoS$_2$-NTs (1.63 μF cm^{-2}) within the same potential range, indicating the TiO$_2$ nanoparticles is very important for the high exposure of MoS$_2$-NTs with effective active sites.

The EIS measurement was also used to investigate the charge transfer resistance (R_{ct}) between the surface of the catalyst and the electrolyte. Fig. 6d showed a comparison of Nyquist plots of

MoS$_2$-NTs, TiO$_2$ and TiO$_2$/MoS$_2$-NTs. It is well known that a smaller arc radius in Nyquist plots indicates a lower interface resistance. Clearly, TiO$_2$/MoS$_2$-NTs showed dramatically decrease of charge transfer resistance than MoS$_2$-NTs or TiO$_2$, indicating that the load of TiO$_2$ can greatly improve the conductivity of the MoS$_2$-NTs by accelerating the electron transport, which promoted the HER activity of TiO$_2$/MoS$_2$-NTs.

Conclusions

In summary, we synthesized a nanocomposite consisting of MoS$_2$ nanotubes loaded with TiO$_2$ nanoparticles and characterized it well from XRD, Raman, XPS, TEM, and HRTEM analysis. TiO$_2$/MoS$_2$-NTs composite showed a high-efficiency electrocatalytic HER comparable to that of MoS$_2$-NTs, as a prominent alternative for platinum-based electrocatalysts, exhibited remarkable HER activity with a relatively low over-potential of 0.21 V at a cathode current density of 10 mA cm^{-2} and a small Tafel slope of 42 mV dec^{-1} as well as excellent long-

term stability. It can be attributed to the high exposure of active sites and fast charge transport simultaneously by the loading with TiO$_2$ nanoparticles. Our research confirmed that electronic and chemical coupling effect between the MoS$_2$ and TiO$_2$ can be utilized in the enhancements of electrochemical performance. Moreover, TiO$_2$/MoS$_2$-NTs composite would be extended to a wide range of energy and environmental applications, such as photocatalytic and photoelectrocatalytic hydrogen production.

Conflicts of interest

There are no conflicts to declare.

Acknowledgements

Notes and references

1 N. Armaroli and V. Balzani, *Angew. Chem., Int. Ed.*, 2007, **46**, 52–66.

2 S. Chen, S. S. Thind and A. C. Chen, *Electrochem. Commun.*, 2016, **63**, 10–17.

3 J. W. Sun, D. K. Zhong and D. R. Gamelin, *Energy Environ. Sci.*, 2010, **3**, 1252–1261.

4 X. X. Zou and Y. Zhang, *Chem. Soc. Rev.*, 2015, **44**, 5148–5180.

5 S. Y. Tee, K. Y. Win, W. S. Teo, L. D. Koh, S. H. Liu, C. P. Teng and Mi. Y. Han, *Adv. Sci.*, 2017, **4**, 1600337.

6 M. C. He, F. P. Kong, G. P. Yin, Z. Lv, X. D. Sun, H. Y. Shi and B. Gao, *RSC Adv.*, 2018, **8**, 14369–14376.

7 E. Kemppainen, A. Bodin, B. Sebok, T. Pedersen, B. Seger, B. Mei, D. Bae, P. C. K. Vesborg, J. Halme, O. Hansen, P. D. Lunda and I. Chorkendorff, *Energy Environ. Sci.*, 2015, **8**, 2991–2999.

8 S. Q. Lu and Z. B. Zhuang, *Sci. China Mater.*, 2016, **59**, 217–238.

9 J. R. McKone, S. C. Marinescu, B. S. Brunschwig, J. R. Winkler and H. B. Gray, *Chem. Sci.*, 2014, **5**, 865–878.

10 A. Eftekhari, *Int. J. Hydrogen Energy*, 2017, **42**, 11053–11077.

11 Y. X. Chen, K. N. Yang, B. Jiang, J. X. Li, M. Q. Zeng and L. Fu, *J. Mater. Chem. A*, 2017, **5**, 8187–8208.

12 C. G. Morales-Guio, L. A. Stern and X. L. Hu, *Chem. Soc. Rev.*, 2014, **43**, 6555–6569.

13 J. Bonde, P. G. Moses, T. F. Jaramillo, J. K. Nørskov and I. Chorkendorff, *Faraday Discuss.*, 2009, **140**, 219–231.

14 J. F. Xie, J. J. Zhang, S. Li, F. Grote, X. D. Zhang, H. Zhang, R. X. Wang, Y. Lei, B. C. Pan and Y. Xie, *J. Am. Chem. Soc.*, 2013, **135**, 17881–17888.

15 J. D. Benck, T. R. Hellstern, J. Kibsgaard, P. Chakthranont and T. F. Jaramillo, *ACS Catal.*, 2014, **4**, 3957–3971.

16 B. Hinnemann, P. G. Moses, J. Bonde, K. P. Jørgensen, J. H. Nielsen, S. Horch, I. Chorkendorff and J. K. Nørskov, *J. Am. Chem. Soc.*, 2005, **127**, 5308–5309.

17 T. F. Jaramillo, K. P. Jorgensen, J. Bonde, J. H. Nielsen, S. Horch and I. Chorkendorff, *Science*, 2007, **317**, 100–102.

18 Q. H. Wang, K. Kalantar-Zadeh, A. Kis, J. N. Coleman and M. S. Strano, *Nat. Nanotechnol.*, 2012, **7**, 699–712.

19 J. Kibsgaard, Z. B. Chen, B. N. Reinecke and T. F. Jaramillo, *Nat. Mater.*, 2012, **11**, 963–969.

20 Z. Lv, N. Mahmood, M. Tahir, L. Pan, X. W. Zhang and J. J. Zou, *Nanoscale*, 2016, **8**, 18250–18269.

21 H. L. Huang, W. H. Huang, Z. H. Yang, J. Y. Huang, J. D. Lin, W. P. Liu and Y. J. Liu, *J. Mater. Chem. A*, 2017, **5**, 1558–1566.

22 S. Jayabal, G. Saranya, J. Wu, Y. Q. Liu, D. S. Geng and X. B. Meng, *J. Mater. Chem. A*, 2017, **5**, 24540–24563.

23 L. Song, M. J. Zhao, X. X. Li, Z. P. Zhang and L. T. Qu, *RSC Adv.*, 2016, **6**, 70740–70746.

24 F. L. Deepak and M. Jose-Yacaman, *Isr. J. Chem.*, 2010, **50**, 426–438.

25 W. J. Jian, X. L. Cheng, Y. Y. Huang, Y. You, R. Zhou, T. T. Sun, J. Xu and X. Wang, *Chem. Eng. J.*, 2017, **328**, 474–483.

26 S. F. Zhuo, Y. Xu, W. W. Zhao, J. Zhang and B. Zhang, *Angew. Chem., Int. Ed.*, 2013, **52**, 8602–8606.

27 J. Wang, J. L. Liu, H. Yang, Z. Chen, J. Y. Lin and Z. X. Shen, *J. Mater. Chem. A*, 2016, **4**, 7565–7572.

28 J. F. Xie, H. Zhang, S. Li, R. X. Wang, X. Sun, M. Zhou, J. F. Zhou, X. W. D. Lou and Y. Xie, *Adv. Mater.*, 2013, **25**, 5807–5813.

29 D. A. Voiry, M. Salehi, R. Silva, T. Fujita, M. W. Chen, T. Asefa, V. B. Shenoy, G. Eda and M. Chhowalla, *Nano Lett.*, 2013, **13**, 6222–6227.

30 B. Seo and S. H. Joo, *Nano Convergence*, 2017, **4**, 19.

31 E. Baran, Z. Baz, R. Esen and B. Y. Devrim, *Appl. Surf. Sci.*, 2017, **420**, 416–428.

32 M. A. Amin, E. M. Ahmed, N. Y. Mostafa, M. M. Alotibi, G. Darabdhara, M. R. Das, J. Wysocka, J. Ryl and S. S. Abd El-Rehim, *ACS Appl. Mater. Interfaces*, 2016, **8**, 23655–23667.

33 W. H. Wang, S. Wang, J. G. Lv, M. Zhao, M. Zhang, G. He, C. X. Fang, L. L. Li and Z. Q. Sun, *J. Am. Ceram. Soc.*, 2018, **101**, 5469–5476.

34 Z. Q. Liu, X. M. Zhang, B. Wang, M. Xia, S. G. Gao, X. Y. Liu, A. Zavabeti, J. Z. Ou, K. Kalantar-zadeh and Y. C. Wang, *J. Phys. Chem. C*, 2018, **122**, 12589–12597.

35 Y. Dong, S. Y. Chen, Y. Lu, Y. X. Xiao, J. Hu, S. M. Wu, Z. Deng, G. Tian, G. G. Chang, J. Li, S. Lenaerts, C. Janiak, X. Y. Yang and B. L. Su, *Chem. - Asian J.*, 2018, **13**, 1609–1615.

36 B. Ma, P. Y. Guan, Q. Y. Li, M. Zhang and S. Q. Zang, *ACS Appl. Mater. Interfaces*, 2016, **8**, 26794–26800.

37 Y. Z. Shen, X. H. Ren, X. Qi, J. Zhou, Z. Y. Huang and J. X. Zhong, *J. Electrochem. Soc.*, 2016, **163**, H1087–H1090.

38 R. Z. Zhang, Q. W. Chen, Y. X. Lei and J. P. Zhou, *J. Mater. Sci.: Mater. Electron.*, 2019, **30**, 5393–5403.

39 M. Zhang, S. Wang, Z. L. Li, C. W. Liu, R. Miao, G. He, M. Zhao, J. Xue, Z. Y. Xia, Y. Q. Wang, Z. Q. Sun and J. G. Lv, *RSC Adv.*, 2019, **9**, 3479–3485.

40 J. G. Lv, R. Miao, M. Zhang, G. He, M. Zhao, B. Yu, W. Wang, B. Li and Z. Q. Sun, *J. Mater. Sci.: Mater. Electron.*, 2018, **29**, 16282–16288.

41 Y. Y. Tian, Y. Song, M. L. Dou, J. Ji and F. Wang, *Appl. Surf. Sci.*, 2018, **433**, 197–205.

42 J. Liang, C. X. Wang, P. Y. Zhao, Y. R. Wang, L. B. Ma, G. Y. Zhu, Y. Hu, Z. P. Lu, Z. R. Xu, Y. Ma, T. Chen, Z. X. Tie, J. Liu and Z. Jin, *ACS Appl. Mater. Interfaces*, 2018, **10**, 6084–6089.

43 X. L. Song, G. F. Chen, L. X. Guan, H. Zhang and J. G. Tao, *Appl. Phys. Express*, 2016, **9**, 095801.

44 M. Nath, A. Govindaraj and C. N. R. Rao, *Adv. Mater.*, 2001, **13**, 283–286.

45 M. Remskar, A. Mrzel, Z. Skraba, A. Jesih, M. Ceh, J. Demsar, P. Stadelmann, F. Levy and D. Mihailovic, *Science*, 2001, **292**, 479–481.

46 X. F. Liu, Z. P. Xing, Y. Zhang, Z. Z. Li, X. Y. Wu, S. Y. Tan, X. J. Yu, Q. Zhu and W. Zhou, *Appl. Catal., B*, 2017, **201**, 119–127.

47 J. Kibsgaard, Z. Chen, B. N. Reinecke and T. F. Jaramillo, *Nat. Mater.*, 2012, **11**, 963–969.

48 J. J. Zhang, M. H. Wu, Z. T. Shi, M. Jiang, W. J. Jian, Z. R. Xiao, J. X. Li, C. S. Lee and J. Xun, *Small*, 2016, **12**, 4379–4385.

49 J. Chen, S. L. Li, Q. Xu and K. Tanaka, *Chem. Commun.*, 2002, **16**, 1722–1723.

50 Q. Wang, J. Y. Huang, H. T. Sun, Y. H. Ng, K. Q. Zhang and Y. K. Lai, *ChemSusChem*, 2018, **11**, 1708–1721.

51 L. X. Zheng, S. C. Han, H. Liu, P. P. Yu and X. S. Fang, *Small*, 2016, **12**, 1527–1536.

52 C. H. Meng, Z. Y. Liu, T. R. Zhang and J. Zhai, *Green Chem.*, 2015, **17**, 2764–2768.

53 W. Wang, Y. Q. Wang, C. P. Li, Y. J. Wu, D. Y. Zhang, K. Q. Hong and Y. M. Sun, *Chem. Commun.*, 2017, **53**, 5461–5464.

54 W. N. Ren, W. W. Zhou, H. F. Zhang and C. W. Cheng, *ACS Appl. Mater. Interfaces*, 2017, **9**, 487–495.

55 C. B. Liu, L. L. Wang, Y. H. Tang, S. L. Luo, Y. T. Liu, S. Q. Zhang, Y. X. Zeng and Y. Z. Xu, *Appl. Catal., B*, 2015, **164**, 1–9.

56 Y. H. Chang, C. T. Lin, T. Y. Chen, C. L. Hu, Y. H. Lee, W. J. Zhang, K. H. Wei and L. J. Li, *Adv. Mater.*, 2013, **25**, 756–760.